Research
A SCIENCE PARTNER JOURNAL

REVIEW ARTICLE

Black Phosphorus for Photonic Integrated Circuits

Mingxin Zhang, Lele Yang, Xiaoxuan Wu, and Junjia Wang *

National Research Center for Optical Sensors/communications Integrated Networks, School of Electronic Science and Engineering, Southeast University, 2 Sipailou, Nanjing 210096, China.

*Address correspondence to: junjia_wang@seu.edu.cn

Citation: Zhang M, Yang L, Wu X, Wang J. Black Phosphorus for Photonic Integrated Circuits. *Research* 2023;6:Article 0206. https://doi.org/10.34133/research.0206

Submitted 24 May 2023
Accepted 19 July 2023
Published 16 August 2023

Copyright © 2023 Mingxin Zhang et al. Exclusive licensee Science and Technology Review Publishing House. No claim to original U.S. Government Works. Distributed under a Creative Commons Attribution License 4.0 (CC BY 4.0).

Black phosphorus gives several advantages and complementarities over other two-dimensional materials. It has drawn extensive interest owing to its relatively high carrier mobility, wide tunable bandgap, and in-plane anisotropy in recent years. This manuscript briefly reviews the structure and physical properties of black phosphorus and targets on black phosphorus for photonic integrated circuits. Some of the applications are discussed including photodetection, optical modulation, light emission, and polarization conversion. Corresponding recent progresses, associated challenges, and future potentials are covered.

Introduction

In the past 30 years, information capacity has grown exponentially, and the large-scale deployment of high-speed communication networks has become an inevitable trend of the globalization process. These put forward higher demands for the technology that meets requirements in terms of capacity and consumption. Photonic integrated circuits are considered to be a promising candidate for next-generation communication systems owing to provide effective solutions with their advantages in transmission speed and energy efficiency. With its integrability with complementary metal oxide semiconductor fabrication, photonic integrated circuits play a crucial role in communication technology [1,2]. Despite substantial advances in high-efficiency and low-cost integrated photonic devices, such as photodetectors [3], sensors [4,5], modulators [6], and light emitters [7], large lattice mismatch and manufacturing complexity are still limiting factors for all integrated solutions.

Two-dimensional (2D) materials have drawn intense attention following the graphene was obtained by mechanical exfoliation of graphite in 2004 [8]. Since then, amazing progress has been made in this field, and they are widely applied in electronics, sensing, energy storage, and photonics (see Fig. 1). Numerous multifunctions and high-performance 2D materials integrated photonic components have been demonstrated by utilizing their advantages over optical and electronic properties, including high specific surface area, broadband absorption, strong light–matter interaction, and easy integration with silicon photonics [9–12]. Graphene, as a widely researched 2D material in recent years, has been demonstrated to be featured with outstanding mechanical strength, high light transmittance, superior carrier mobility, and high thermal conductivity [13–17]. However, optoelectronic applications of graphene are constrained by its zero bandgap, which leads to large dark current. Transition-metal dichalcogenides also present attractive properties, but their relatively wide bandgaps lead to very limited bandwidths and restricting their optoelectronic applications. In addition, the insertion loss is extremely high when the device is operating near the resonance wavelengths [18].

Black phosphorus (BP) has attracted considerable interest in catalytic systems, biomedicine, energy storage systems, catalytic systems, flexible sensors, and photonic integrated circuits over the past 10 years [19–26]. Although the first BP synthesis by Bridgman at 1.2 GPa and 200 °C can be traced back to the mid-1910 [27], there was not much interest in the material itself at that time. At the beginning of 2014, BP was restudied from the perspective of 2D materials [28] due to its exceptional physical characteristics including direct and tunable bandgap, relative high carrier mobility, and anisotropic properties [29–34].

Originally, BP was mostly synthesized by the high-pressure method [35]. Later, the synthesis processes of BP can be divided into bottom-up and top-down approaches. Bottom-up approaches like pulsed laser deposition and chemical vapor transport methods are commonly used for large-scale production [36–38]. However, the complex processes and high costs limit its feasibility to prepare the monolayer BP with high quality. Recently, Chen et al. [32] utilized controllable sustained vapor growth method to prepare large-scale BP thin film with high crystallinity and purity. The widely used top-down approaches for preparing few-layer BP with large lateral size are liquid exfoliation and mechanical exfoliation [39]. In order to improve the production rate, Zhang and co-workers [40] reported an intermediate-assisted grinding exfoliation to prepare various 2D layer materials, like monolayer or few-layer BP.

The BP bandgap is reduced from ~2 eV for a monolayer to ~0.3 eV for bulk materials because of the vertical quantum confinement effect [41,42]. As can be seen in Fig. 1, such a layer-tunable bandgap covers a wide electromagnetic spectral range from visible to mid-infrared (mid-IR) and bridges the gap between graphene and other 2D materials. Furthermore, BP bandgap is

sensitive to a vertical electric field and can be efficiently tuned by electrical gating. Another important property is the saturable absorption, which may realize high-performance all-optical modulation. BP also preserves remarkable electrical performance, such as high carrier mobility up to 5,200 $cm^2 V^{-1} s^{-1}$, high on-off ratio exceeding 10^5, and high saturation current in field-effect transistors [43–45]. The puckered arrangement of P atoms results in asymmetric crystal structure, which gives rise to its unique in-plane anisotropic electrical, thermal, and optical properties [46–48]. These extraordinary features make BP a very promising 2D material for diverse photonic applications, including wavelength converters [49], photodetectors [50], switches [51], modulators [52], and lasers [53]. BP is sensitive to some environmental factors such as oxygen and water [54,55]. Encapsulation [56], ligand surface coordination [57], doping [58], synchronous fluorination [59], covalent functionalization [60], and other strategies in the process of the fabrication have been presented to avoid degradation of BP and achieve excellent long-term stability. For example, Liu et al. [61] proposed a powerful short-distance transport growth method to enhance ambient stability by doping of various elements. Up to now, the most promising approach in practical application is to encapsulate with suitable materials such as aluminum oxide and packaging in inert atmosphere.

In this review, we briefly introduce the research advances of BP for photonic integrated circuits in recent years. First, the lattice structure and physical properties of BP are described. Subsequently, we focus on the applications of BP and their proceedings in photodetection, electro-optic (EO) modulation, all-optic modulation, light emission, and polarization conversion. Finally, based on BP current progress, current challenges and future prospects are highlighted.

BP Structure and Properties

Single-layer BP consists of a corner-sharing puckered honeycomb crystal structure where each phosphorus (P) atom is surrounded by three adjacent P atoms. Different from graphene, five outer shell electrons from a P atom are bonded to three outer shell electrons from other through sp^3-hybridized orbitals [62]. However, this structure results in the remaining lone-pair electrons being easily oxidized in the air, which

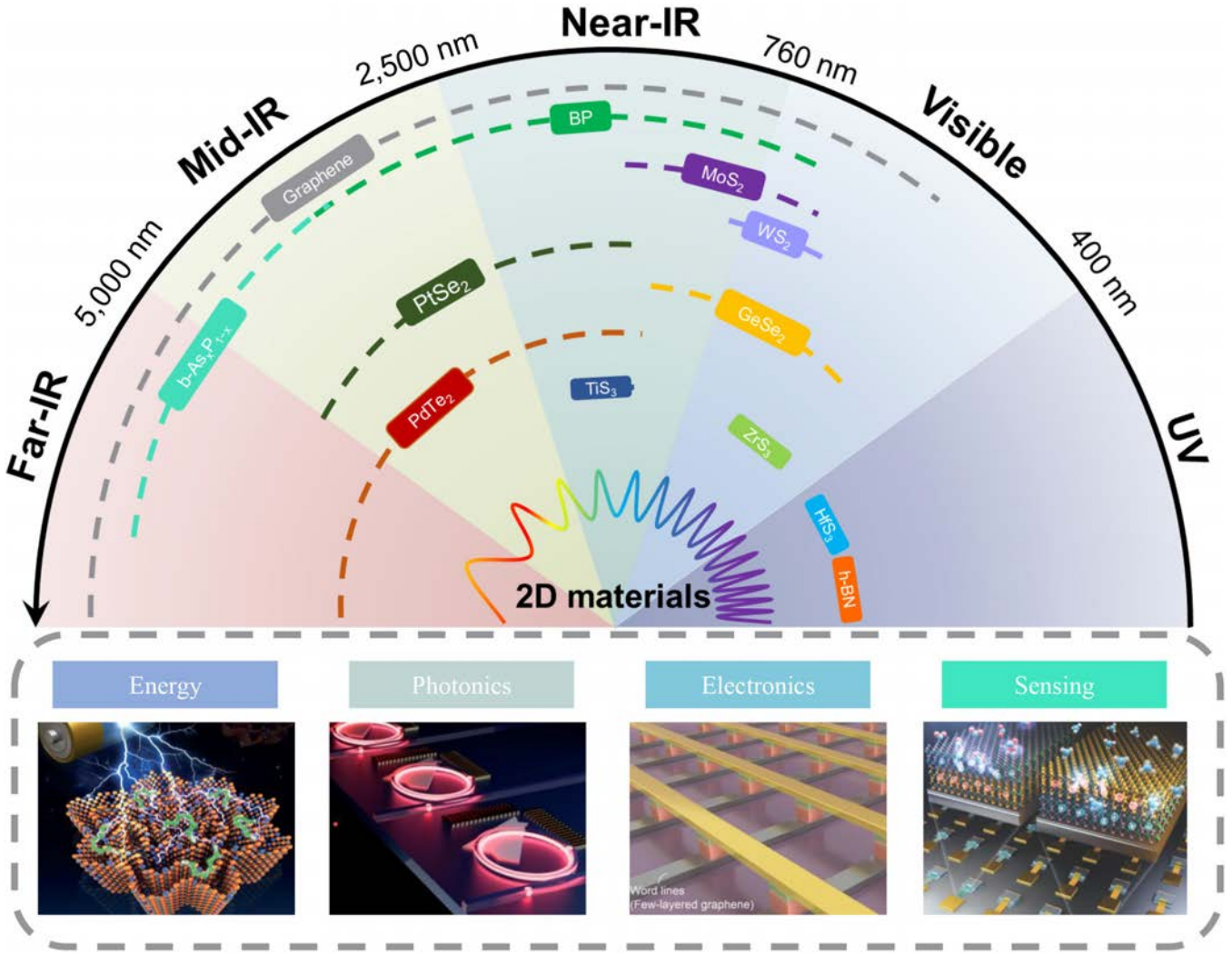


Fig. 1. Comparison of the response range for various 2D materials and their potential applications. All images reproduced with permission: "Energy" from [129]. Copyright 2018 Wiley-VCH. "Photonics" from [130]. Copyright 2022 American Chemical Society. "Electronics" from [131]. Copyright 2023 Wiley-VCH. "Sensing" from [132]. Copyright 2020 Wiley-VCH. UV, ultraviolet.

seriously affects BP properties and induces degradation of device performance. As shown in Fig. 2A, the distance between neighboring BP layers is only 0.53 nm, so that the single or fewer layers of BP film can be obtained from bulk crystal by mechanical or liquid exfoliation [63,64]. The monolayer folded along the x-direction contains two types of chemical bonds. The longer bond connecting two P atoms between the top and bottom in a monolayer has a bond length of 0.2244 nm. Another shorter bond connecting the two P atoms in the same plane has a bond length of 0.2224 nm [65,66]. From the z-direction view, the BP lattice displays a hexagonal structure with two types of bond angles. The smaller bond angle of 96.3°consists of 1 short bond and 1 long bond, and the larger bond angle of 102.1° consists of two short bonds (Fig. 2B). Thickness dependence of the BP bandgap is definite: it monotonically increases from a narrow bandgap (about 0.3 eV) for bulk to a large gap (about 2 eV) for monolayer, owing to the stronger coupling of interlayer electronic state contrast to other 2D materials [67]. The widely tunable and direct bandgap from the bulk down to monolayer make BP particularly suitable for efficient photodetection and light emission. Several researchers have experimentally measured and theoretically demonstrated the thickness-dependent of BP by IR, photoluminescence (PL), and scanning tunneling spectroscopy [28,42,64,68–74], as shown in Fig. 2C. By alloying BP with arsenic, Liu et al. [75] reported a black arsenic-phosphorus (b-As_xP_{1-x}) with tunable bandgaps in the range of 0.3 to 0.15 eV, confirming that the bandgap of the BP can be further modified.

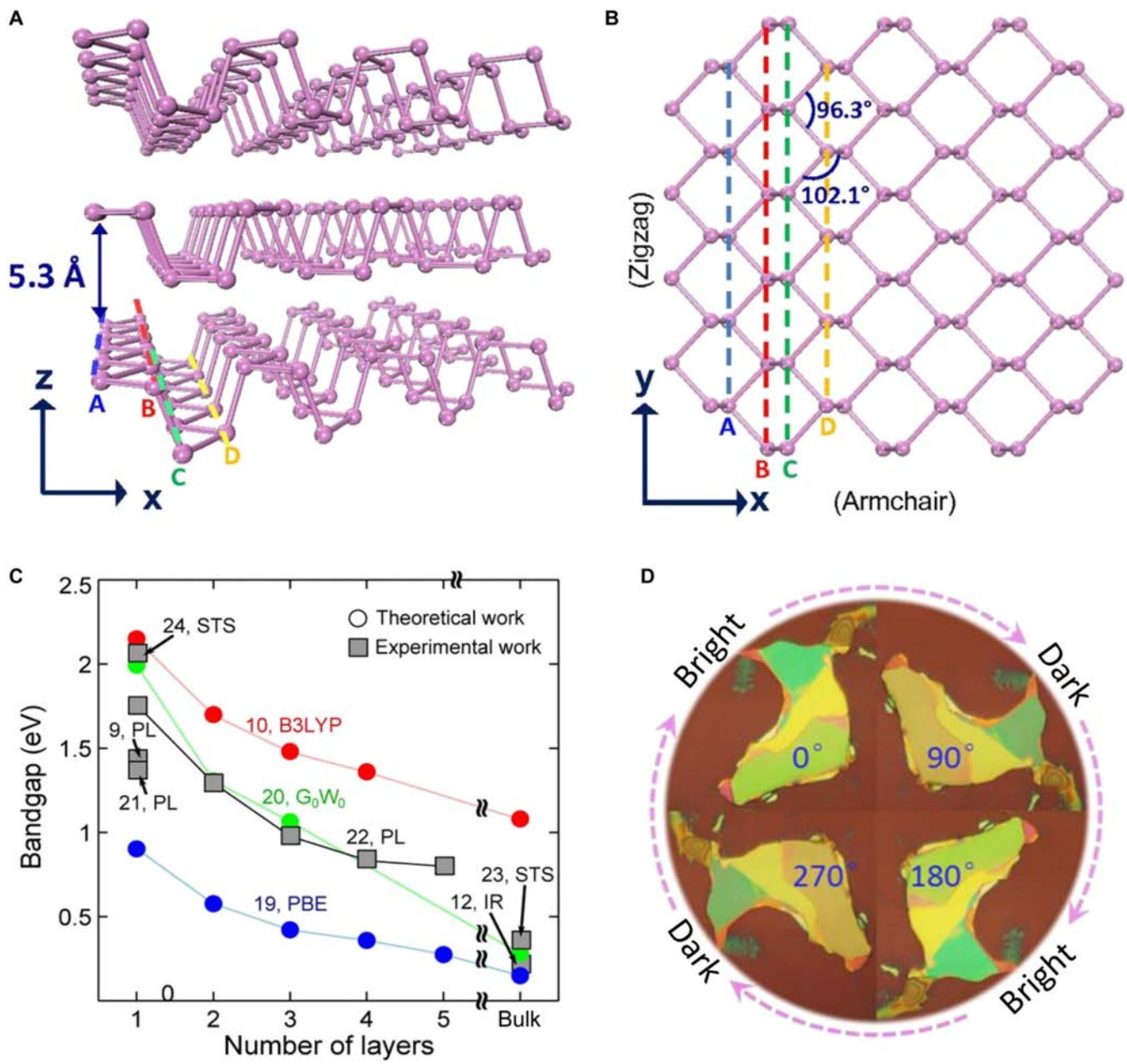


Fig. 2. (A) Side view and (B) top view of the BP crystal structure. Reproduced with permission from [63]. Copyright 2015 National Academy of Sciences. (C) The BP bandgap as a function of layer numbers calculated by different methods. B3LYP, Becke, 3-parameter, Lee–Yang–Parr; G_0W_0, Green's function and a screened Coulomb interaction; PBE, Perdew–Burke–Ernzerho; STS, scanning tunneling spectroscopy. Reproduced with permission from [64]. Copyright 2015 American Chemical Society. (D) Optical images of few-layer BP with different rotation angles. Reproduced with permission from [79]. Copyright 2017 American Chemical Society.

The key characteristic that distinguishes BP from other 2D materials is unique anisotropy, which is evident in its crystal structure [76,77]. The zigzag and armchair directions are parallel and perpendicular to the atomic ridge, respectively. Strong structural anisotropy caused by these two inequivalent orientations in the BP lattice is the reason that makes its unique in-plane anisotropy for thermal, electrical, and optical characteristics. Angle resolved absorbance, Raman spectroscopy, and PL spectra are commonly method to reveal BP optical anisotropic properties. Ling et al. [78] demonstrated the in-plane optical anisotropy of BP samples through angle resolved absorbance. The electron–phonon interaction is related to the crystalline orientation of BP samples. Mao et al. [79] utilized polarized optical microscopy to research optical anisotropy of few-layer BP under the white light illumination, as shown in Fig. 2D. The evidence shows that the difference between the real and imaginary refractive indices along two directions is what causes optical anisotropy of BP. Wu et al. [80] identified orientation of BP samples using Raman spectroscopy. When the incident light is parallel to the armchair (or zigzag) direction, the local maximum (or minimum) of Ag^2 mode intensity is achieved. Alodan et al. [81] observed highly anisotropic PL of BP nanosheets in the wavelength range from 590 to 720 nm.

BP for Photodetection

Photodetectors, as the devices that convert light into electrical signal, have attracted immense research interest in many fields. BP has been demonstrated to be a promising 2D semiconductor for visible to mid-IR photodetectors due to its unique properties. The wide spectral responsivity offers a new opportunity for broadband photo detection [82]. The BP exhibits great differences in carrier mobility and optical absorbance along the zigzag and armchair directions due to strong in-plane anisotropy. The increase of BP thickness also greatly improves the optical absorption. This indicate that the crystalline orientation and thickness of the BP play crucial roles on the responsivity and bandwidth of the photodetectors. [83–85]. There are two categories of mechanisms for 2D materials photodetection, the photon-related detection mechanisms (including photoconductive effect, photovoltaic effect, and photogating effect) and thermal-related mechanisms (including photo-thermoelectric effect and bolometric effect), as shown in Fig. 3A. The photoconductive effect and photovoltaic effect serve as primary mechanisms for integrated BP photodetector. The incident photons induce electron-hole pairs and increases carrier concentration and conductivity in the semiconductor material. With an applied bias voltage, the photogenerated electron-hole pairs are separated and move respect to the electric field, and then comes photocurrent generation by photoconductive effect [86]. For photovoltaic effect, photogenerated electron-hole pairs are separated according to the electric fields in the semiconductor depletion region. The intrinsic electric field is usually generated by the noticeable difference of work function between two materials, such as p-n junctions and Schottky barrier junctions [87]. Despite the photon-related detection mechanisms systematically described above, to realize high responsivities and large bandwidths simultaneously remains a huge challenge. Researchers proposed various structures to increase the responsivity of BP-based photodetectors.

Youngblood et al. [88] utilized few-layer BP to design a waveguide-integrated and gate-tunable photodetector for near-IR telecom band. The performance of the BP photodetector is optimized by integrating a field-effect transistor on the waveguide to induce doping on the BP layer. Compared with graphene counterparts, the dark current in BP photodetectors is drastically decreased when the BP are of low doping, where the photovoltaic effect dominates. Additionally, the device exhibits an excellent responsivity of 657 mA/W at room temperature using a 100-nm thickness of BP.

Further miniaturization of the photodetector increases responsivity, response speed, and internal quantum efficiency. However light–matter interaction lengths are relatively reduced, which limits the BP light absorption. In order to enhance the responsivities in integrated-waveguide BP photodetectors, Ma et al. [89] designed a slow-light-enhanced Mid-IR photodetector on the photonic crystal (PhC) waveguide (WG) with a length of 10 μm, as shown in Fig. 3B. The enhancement of the slow light is verified and characterized through the shared-BP photonic systems including two BP photodetectors fabricated by a PhC WG and a spatially close subwavelength grating waveguide, respectively. The photocurrent is dominated by the photoconductive effect. The BP photodetector based on the PhC WG exhibits a high responsivity (11.31 A/W) and a low noise-equivalent power (0.012 nW $Hz^{-1/2}$) at a bias voltage ~0.5 V.

Liu and co-workers [90] reported a high-responsivity avalanche photodetector based on the plasmonic enhanced BP integrated on silicon waveguide at wavelengths of 1.55 and 1.95 μm, as shown in Fig. 3C. This device consists of two nanoslots between the ultrathin silicon waveguide at the middle and two metal contacts on both sides. This waveguide structure not only facilitates the light–BP interaction but also reduces carrier transit time. Owing to the photovoltage effect in BP, the avalanche photodetector achieves a high responsivity of 125 A/W at the wavelength of 1.95 μm and a 3-dB bandwidth of 1.05 GHz.

Another strategy is to use 2D van der Waals heterostructures to enable photodetection with high dark current suppression. As shown in Fig. 3D, Chen et al. [91] reported a mid-IR photodetector using BP/$MoTe_2$ van der Waals heterostructure to realize high-performance photodetection. Scanning photocurrent mapping demonstrates that the photovoltaic response mainly derived from the BP/$MoTe_2$ heterojunction rather than from the Schottky junction. They reported response and recovery of ~30 and ~58 ns under the laser illumination of ~6.7 μW nm, which are much faster than those of In_2Se_3-based photodetectors.

The thin-film lithium niobate (TFLN) platform provides a new way for photonic integrated circuits, attributing to excellent crystalline properties and optoelectronic features of TFLN. As shown in Fig. 3E, Xue et al. [92] reported a high-speed integrated BP photodetector based on the TFLN waveguide. The trap-induced photoconductive gain is considered as dominant photoresponse mechanism. Benefiting from the higher index contrast, the integrated-waveguide BP photodetector exhibits a high absorption coefficient of 1.56 dB/μm and a high responsivity of 2.64 A/W. A 3-dB bandwidth of 1.97 GHz has also been measured.

We summarize various integrated BP-based photodetectors, and their performance metrics are highlighted in Table 1 [82–85,88–92]. For gate-tunable photodetector, low dark current can be realized by integrating a field-effect transistor on the waveguide to induce low doping. Benefiting from the enhanced light–matter interactions, PhC WG, chalcogenide

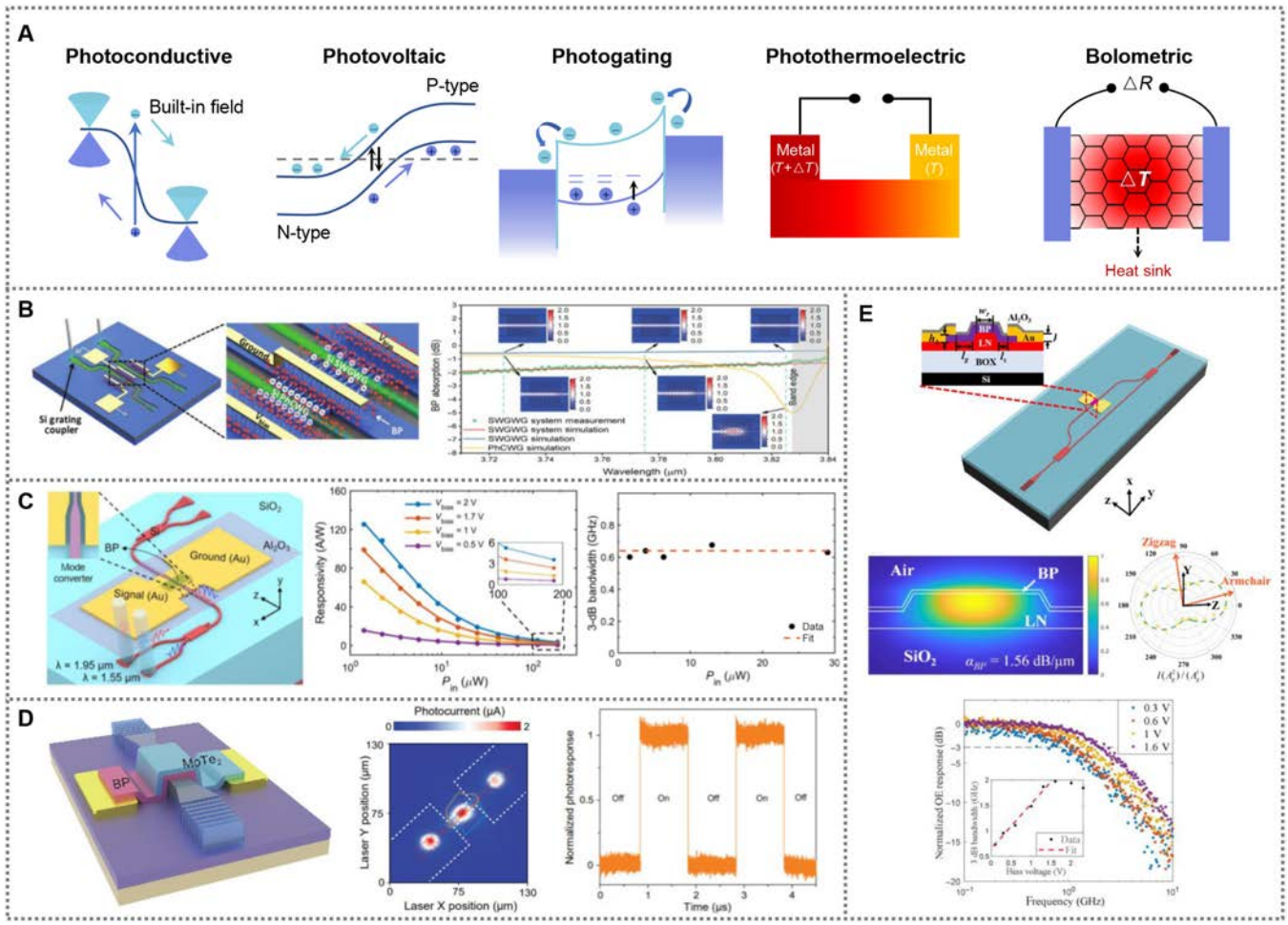


Fig. 3. (A) Different photocurrent generation mechanisms: photovoltaic effect, photogating effect, photothermoelectric effect, and bolometric effect. (B) A slow-light-enhanced photodetector based on the PhC WG for mid-IR. Reproduced with permission from [89]. Copyright 2020 Wiley-VCH. (C) A novel avalanche photodetector based on the BP/silicon hybrid plasmonic waveguide operating at wavelengths of 1.55 and 1.95 μm. Reproduced with permission from [90]. Copyright 2022 American Chemical Society. (D) A mid-IR photodetector based on the BP/$MoTe_2$ van der Waals heterostructure. Reproduced with permission from [91]. Copyright 2022 American Chemical Society. (E) An integrated BP photodetector based on the TFLN waveguide. Reproduced with permission from [92]. Copyright 2022 Optica Publishing Group.

glass waveguide, and TFLN waveguide significantly enhance the responsivity of photodetectors. Furthermore, heterostructures formed by BP and other 2D materials not only increases the response speed but also reduces dark current.

BP for Optical Modulation

The performance of optical modulators can be characterized by several parameters including modulation speed, modulation depth, and energy consumption. These parameters can be regulated by applied external fields such as electric fields, optical fields, and magnetic fields. Although relative higher modulation depth can be easily realized by electro-optical modulation, the energy consumption and modulation speed are still limiting factors. All-optical modulation without electro-optical conversion increases the modulation speed and realizes lower power consumption with larger bandwidth. However, the modulation depth still needs to be improved [93]. Magneto-optic modulation is realized by using external magnetic field to control optical response, has received as less attention as electro-optical or all-optical method modulation, but could be useful for deep ultraviolet applications [94].

All-optical modulation

Optical modulators are devices that tune the amplitude or phase of the light by applying light or electric field. All-optical modulators play a crucial role in high-speed photonic systems. BP is a broadband saturable absorbing material at the wavelengths from visible to mid-IR, which can be used in all-optical modulation and pulsed light generation [95,96]. Saturable absorption is a nonlinear optical phenomenon caused by Pauli-blocking effect, which occurs under high intensity of light [97]. As shown in Fig. 4A, when the energy of the incident light is greater than the bandgap of the material, photons can be absorbed and, in turn, electrons in the valence band are excited into conduction band. As the light intensity increases to a relatively high level, the number of the photocarriers increases above the threshold. At the same time, the conduction band cannot accept any more incoming electrons and the absorption is reduced [98].

Wang et al. [99] demonstrated a novel all-optical BP modulator with a fiber Mach–Zehnder interferometer structure, as shown in Fig. 4B. To improve its long-term environmental stability, BP was prepared by an electrochemical exfoliation

Table 1. A comparison of the various BP photodetector metrics.

Structure	Wavelength (nm)	T_{BP} (nm)	Responsivity (A/W)	3-dB Bandwith (GHz)	Detection mechanisms	Reference
Al_2O_3/BP/SiO_2/P-Si	400–3,800	30	6	N/A	Photoconductive	[82]
BP/ChG waveguide	2,185	8.3	0.04	N/A	Photovoltaic	[83]
Al_2O_3/BP/SOI	3,680	40	23	N/A	Photoconductive	[84]
Al_2O_3/BP/SOI	2,000	40	0.3067	1.33	Photovoltaic	[85]
BP/SOI	1,570–1,580	100	0.657	2.8	Photovoltaic	[88]
BP/PhC WG	3,825	40	11.31	0.00055	Photoconductive	[89]
BP/Al_2O_3/SOI	1,550–1,950	30	125	1.05	Photovoltaic	[90]
BP/$MoTe_2$/SOI	3,000–3,900	25	0.85	N/A	Photovoltaic	[91]
Al_2O_3/BP/TFLN	1,550	39.8	2.64	1.97	Photoconductive	[92]

N/A, not applicable; ChG, chalcogenide glass.

method and then simultaneously fluorinated in an electrochemical exfoliation. After reaction, few-layer fluorinated phosphorene was deposited onto a microfiber using optical deposition approach. When the controlling light is coupled into fluorinated-phosphorene-deposited microfiber, the fluorinated phosphorene could absorb the light and increase surface temperature, which results in a phase shift in signal light. The maximum phase shift of the phase modulator is 8π, and the maximum interference contrast is 17 dB with a control light power of 290 mW.

In order to enhance the performance of all-optical modulators, integrating the saturable absorber materials on silicon waveguide is an effective way. As shown in Fig. 4C, Cheng et al. [100] integrated a BP thin film on silicon micro-ring resonators, realizing a BP-integrated all-optical modulator. BP with a thickness of 22 nm was exfoliated and transferred onto the ring resonator by a transfer print method. The temporal and frequency responses of the modulator were observed when both the pump and the probe light were coupled into the waveguide. Based on the photo-thermal effect, the BP-integrated all-optical modulator exhibited better performance including faster response time (rise time of only 479 ns and decay time of 113 ns), broader 3-dB bandwidth (about 2.5 MHz), and higher tuning efficiency (0.164 π/mW), compared to fiber-based all-optical modulators. This work established an alternative strategy for developing integrated all-optical modulators.

EO modulation

EO modulator is one of the most important components in photonic integrated circuits. It has advantages over other types of modulators in terms of optical loss, power consumption, and speed [101]. Electrorefractive modulators tune the real part of the refractive index by applying an electric field. On the contrary, the electroabsorptive modulators tune the imaginary part of the refractive index by applying an electric field.

The EO modulation in BP is dominated by quantum constrained Franz–Keldysh effect and Burstein–Moss effect, as shown in Fig. 5A. With an out-of-plane electric field, the electronic bands in BP exhibit a relative bending. It brings valence band maximum and conduction band minimum closer. The reduction of effective bandgap facilitates BP to absorb photon energies with broader range. This modification of BP optical response can be described by the quantum-confined Franz–Keldysh effect, enabling efficient EO modulations [102]. The Burstein–Moss effect is a change in bandgap of the semiconductor resulting from band filling. By applying an external gate bias voltage, the increase of charge carrier density reduces the available unoccupied electronic states. This leads to a decrease in optical conductivity at the transition energy [103,104]. Unlike the quantum-confined Franz–Keldysh effect, the Burstein–Moss effect broadens the effective optical bandgap in BP.

Using scanning tunneling microscopy, Liu et al. [105] observed bandgap reduction in BP flakes, induced by a giant Stark effect by electrostatic gating, as shown in Fig. 5B. Experimental results show that BP bandgap monotonically reduces with increasing electric field intensity, which is due to band filling. In an 11-layers BP flake, the bandgap shrinks to 75% when applying a field intensity of 0.1 V/nm.

Peng et al. [106] reported a mid-IR BP EO modulator using a silicon substrate as a back gate with normal incident light, as shown in Fig. 5C. They further studied its EO modulation ability by taking advantage of the quantum confined Franz–Keldysh effect. The EO modulation exhibits clear dependence on the BP thickness and gate voltage. Strong intensity modulation can be observed at different photon energies of 0.38, 0.43, and 0.5 eV when photon energy are continuously scanned. In addition, a strong layer correlation is also observed by comparing 9- and 12-nm-thick BP samples. The two modulation mechanisms need to be further studied. Lin et al. [107] reported that operating BP in the Burstein–Moss effect and quantum-confined Franz–Keldysh effect can greatly improve electro-absorption as well as power efficiency. The relative contribution of the Burstein–Moss effect and quantum-confined Franz–Keldysh effect is related to the doping range and multilayer BP thickness.

To further improve the extinction ratio, Huang et al. [108] integrated BP on silicon waveguide to construct an EO modulator for the mid-IR ranging from 3.85 to 4 μm, as shown in Fig. 5D. The signal is modulated by gating the BP with a top

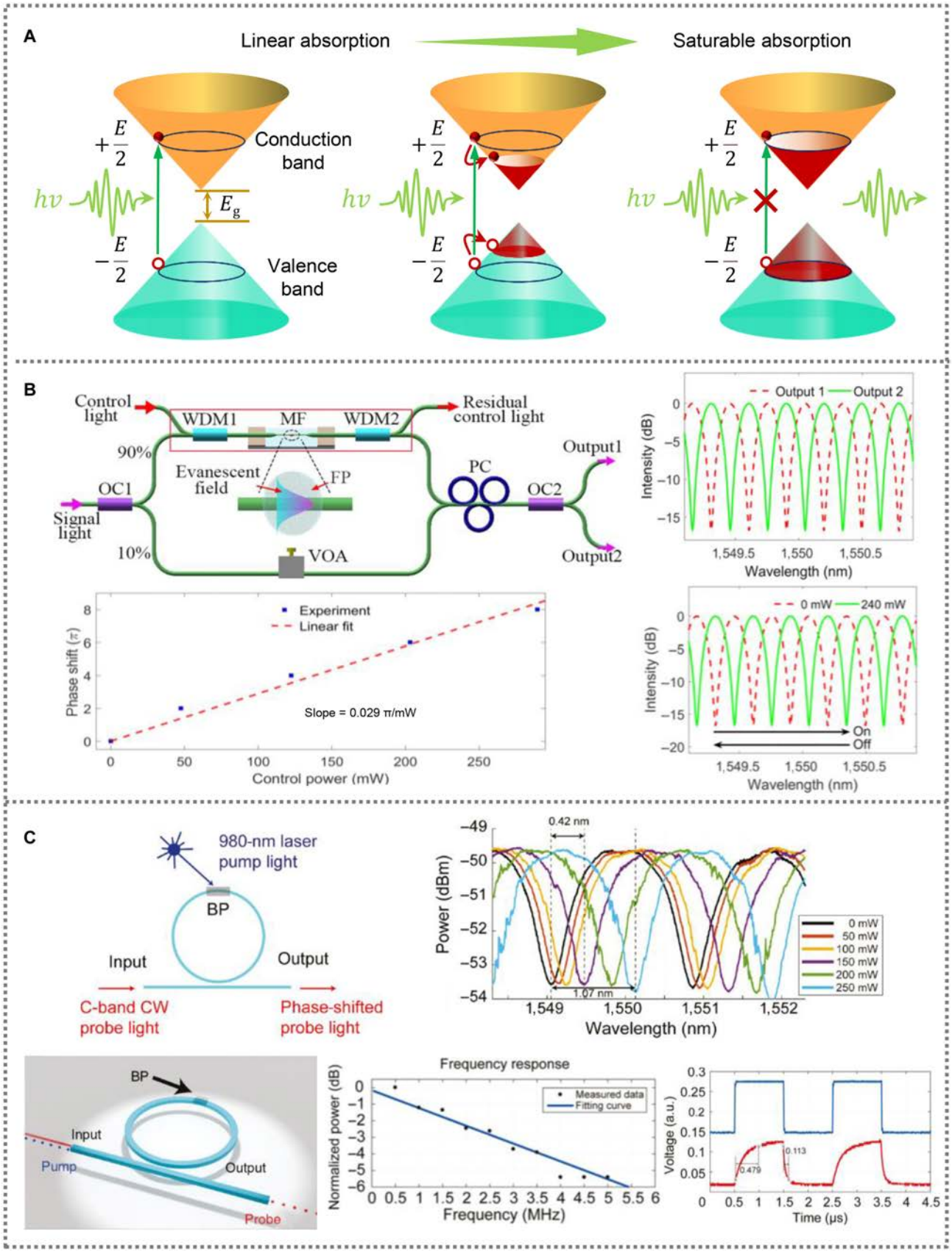


Fig. 4. (A) Schematic for saturable absorption. (B) A fiber-based all-optical modulator based on a Mach–Zehnder interferometer structure consisting of few-layer fluorinated phosphorene. OC1 and OC2, two optical fiber couplers; WDM1 and WDM, two wavelength division multiplexers; MF, microfiber; VOA, variable optical attenuator; PC, polarization controller; FP, fluorinated phosphorene. Reproduced with permission from [99]. Copyright 2017 Wiley-VCH. (C) An integrated all-optical modulator based on BP thin film and micro-ring resonators. CW, continuous wave. Reproduced with permission from [100]. Copyright 2020 Walter de Gruyter Foundation.

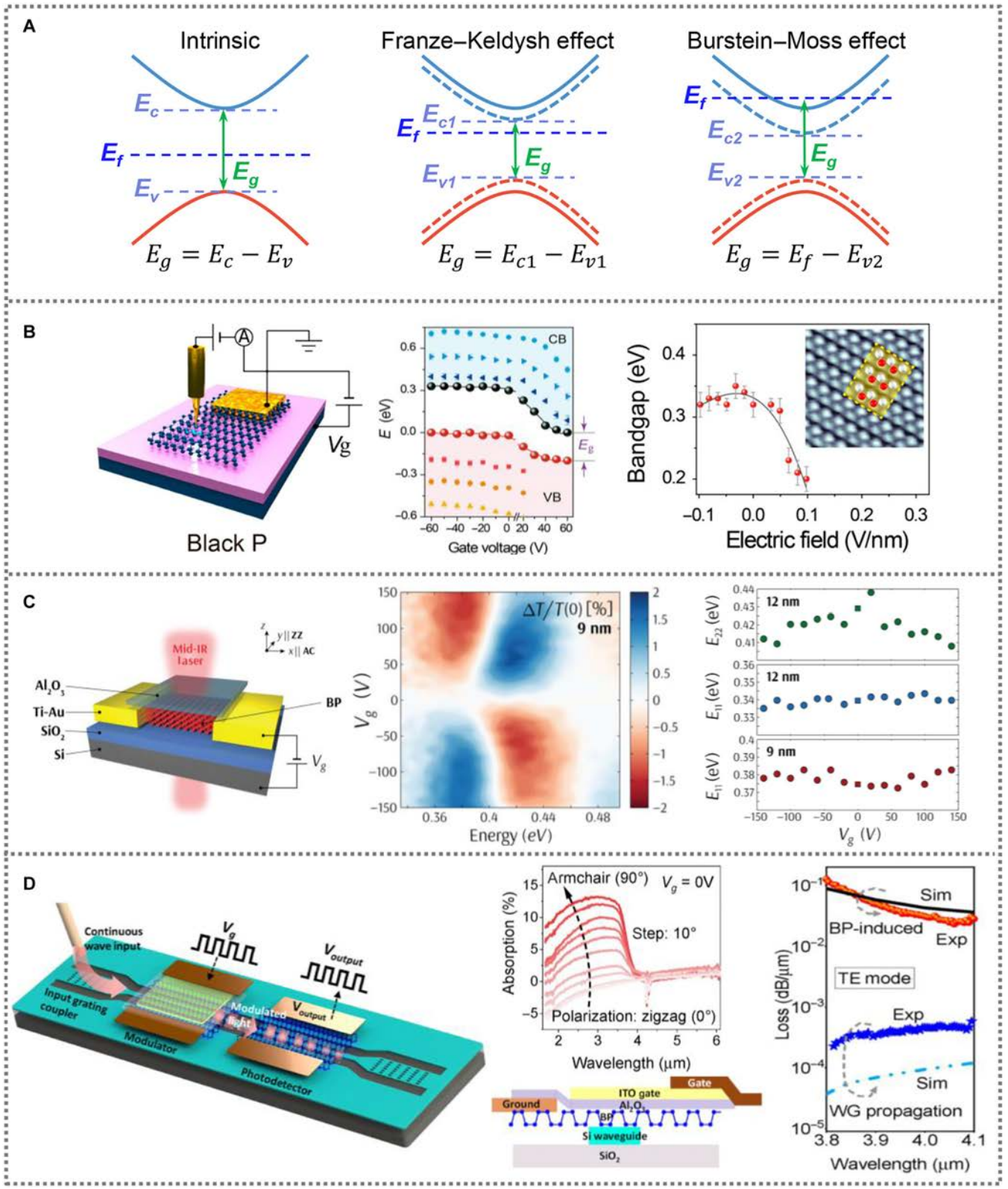


Fig. 5. (A) Schematic for Franze–Keldysh and Burstein–Moss effect. (B) Stark effect in electrostatically gated few-layer BP observed by low-temperature scanning tunneling microscopy. Reproduced with permission from [105]. Copyright 2017 American Chemical Society. (C) An EO modulator with multilayer BP for the mid-IR range. Reproduced with permission from [106]. Copyright 2017 American Chemical Society. (D) Hybrid integration of mid-IR EO modulator on silicon waveguide. TE mode, transverse electric mode. Reproduced with permission from [108]. Copyright 2021 Elsevier.

Table 2. A comparison of the various BP EO modulator metrics.

Structure	Wavelength (nm)	T_{BP} (nm)	Modulation depth (dB)	Modulation mechanisms	Reference
Al_2O_3/BP/SiO_2/Si	2,500–3,700	9	5	Franz–Keldysh	[106]
Al_2O_3/BP/SOI	3,300	20	N/A	Burstein–Moss and Franz–Keldysh	[107]
ITO/Al_2O_3/BP/SOI	3,850–4,100	20	5	Burstein–Moss and Franz–Keldysh	[108]

gate by a combination of the Burstein–Moss and Franz–Keldysh effects. The modulation depth of ~5 dB is achieved at a bias voltage of −4 V with a footprint of 225 μm^2. The 3-dB bandwidth of the modulator exhibits an upward trend until it saturates at around 400 kHz with the increase of wavelength from 3.85 to 4.1 μm, which would be sufficient for sensing requirement of on-chip mid-IR systems.

We compare various BP-based EO modulators, as shown in Table 2 [106–108]. The Burstein–Moss effect and quantum-confined Franz–Keldysh effect improve the modulation depth efficiently.

BP for Light Source

Light emitter is widely used in the field of communication [109], sensing [110], and medical treatment [111]. The operating wavelength of a light emitter depends on the bandgap of the material. Similar to the BP-based photodetectors, the light emitters also display strongly anisotropic properties. The polarized emission along the armchair and zigzag crystal direction reaches maximum and minimum, respectively. The tunable bandgap makes BP a potential light-emitting material in constructing multifunctional IR light emitters [112,113].

Wang et al. [114] proposed a room-temperature light-emitting diode based on the BP/MoS_2 heterojunction prepared by mechanically exfoliated method (Fig. 6A), showing polarized electroluminescence (EL). Under a forward bias voltage of $V_{DS} = 7$ V, the EL has a wavelength of 3.68 μm, and the internal quantum efficiency and external quantum efficiency are calculated to be 0.03% and 1%, respectively.

Chang et al. [115] integrated a BP mid-IR light emitter on silicon waveguide using graphene as transparent contacts, as shown in Fig. 6B. Under forward bias, the hBN/Gr_T/BP/Gr_B heterostructures light-emitting diode emits polarized EL at $\lambda = 2.5$ μm and $\lambda = 3.5$ μm, with external quantum efficiencies of 80% and 0.084%, respectively.

Owing to the actively tunable bandgap property, Kim et al. [116] demonstrated room-temperature tunable IR BP light-emitting diodes by straining the substrate. PL spectroscopy shows that the PL intensity increases with the enhancement of material strain, and the EL increases with the PL quantum yield. The internal quantum efficiency of BP light emitter varies from 0.73% (0.2%; compressive) to 2.47% (1.0%; tensile) due to its highly strain-sensitive nature.

Interestingly, the peak position of the EL and PL spectra both shows an anomalous blueshift with increasing temperature [117,118]. This phenomenon can be attributed to the mechanical strain effect induced by lattice thermal expansion at higher temperatures, which leads to the monotonic increase of the BP bandgap with temperature. The temperature dependence of BP provides a promising strategy for tuning waveguide-integrated BP-based light emitters.

Overall, scientists proposed various light emitters based on BP with different structures, and their key parameters are summarized in Table 3 [114–120]. In addition to the in-plane anisotropy and thickness dependency, the temperature dependency and strain dependency of BP are the key factors affecting performance of the light emitters. Light emission can be greatly improved by integrating BP or its heterostructure on the integrated photonic structures, such as Al_2O_3/Au optical cavities or silicon photonic waveguides.

BP for Polarization Conversion

The anisotropic crystal structure makes BP a competitive candidate for polarization manipulation [121]. Polarization is one of the fundamental physical features of light and is widely used in many fields [122–125]. BP has excellent electrically tunable optical dichroism, which can directly respond to polarized light, ensuring the development of polarization-sensitive optoelectronic devices.

Biswas et al. [126] proposed a reconfigurable polarization converter by integrating the trilayer BP onto an optically resonant cavity for telecommunication wavelengths ranging from 1,410

Table 3. A comparison of the various BP light emitter metrics.

Structure	Wavelength (nm)	T_{BP} (nm)	Internal quantum efficiencies (%)	Eternal quantum efficiencies (%)	Reference
BP/MoS_2	3,680	70	0.03	1	[114]
hBN/Gr_T/BP/Gr_B	3,500	65	N/A	0.084	[115]
BP/MoS_2/PETG	5,500	20	0.73–2.47	N/A	[116]
hBN/BP	2,800–4,000	46	N/A	N/A	[117]
BP/WSe_2	2,790	6	N/A	N/A	[118]
BP/Al_2O_3/Au	3,650	80	N/A	4.43	[119]
BP/MoS_2/b-$As_{0.46}P_{0.54}$	2,500–6,000	20	N/A	0.3	[120]

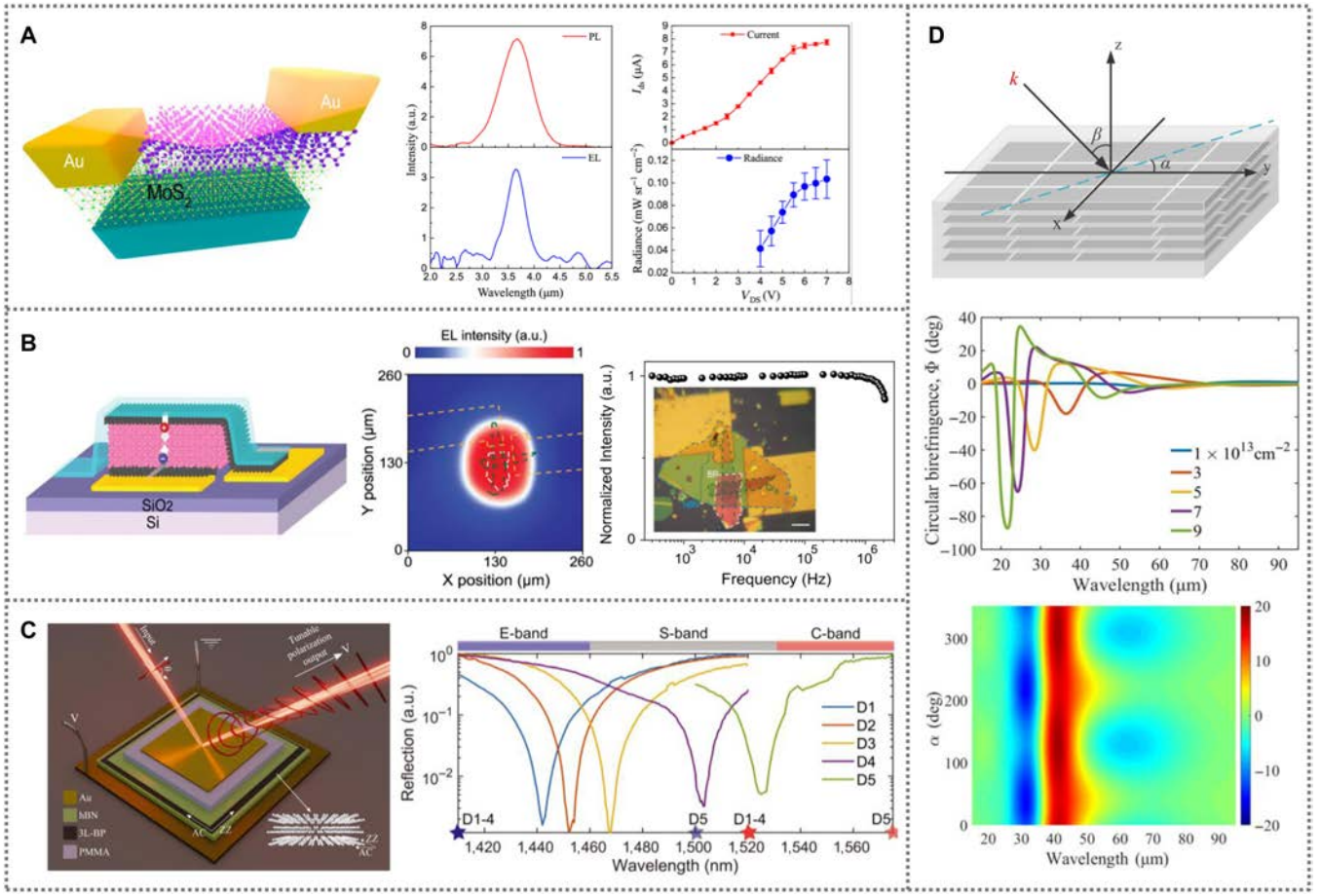


Fig. 6. (A) A mid-IR light-emitting diode based on the BP/MoS_2 heterojunction. Reproduced with permission from [114]. Copyright 2020 American Chemical Society. (B) A mid-IR light-emitting diode based on the hBN/Gr_T/BP/Gr_B heterostructures. Reproduced with permission from [115]. Copyright 2020 American Chemical Society. (C) A trilayer BP heterostructure integrating in a Fabry–Pérot cavity for polarization conversion. Reproduced with permission from [126]. PMMA, polymethyl methacrylate. Copyright 2022 American Association for the Advancement of Science. (D) A twisted multilayer BP structure and its optical responses to circularly polarized light. Reproduced with permission from [128]. Copyright 2022 Optica Publishing Group.

to 1,575 nm. The cavity is formed between a high-reflectivity gold mirror and a partial-transmitting thin gold mirror, as shown in Fig. 6C. The trilayer BP is encapsulated by hexagonal boron nitride, and different thickness of polymethyl methacrylate is used to adjust the cavity resonance frequency. The polarization conversion spans nearly half the Poincaré sphere by electrical tuning. Matthaiakakis et al. [127] reported an approach to realize tunable polarization conversion without asymmetric and chiral nanostructure. The dynamic polarization conversion from linearly polarized light to circularly polarized light can be achieved by altering ellipticity of the scattered wave. Hu et al. [128] proposed a multilayer twisted BP stack, as illustrated in Fig. 6D. Circular dichroism and circular birefringence responses are studied. The twisted BP stacks make it possible to enable giant tunability in polarization.

The polarization conversion based on the BP has been made progress in structure design and integration method. However, how to further improve the dynamic range and active control are problems to be solved.

Conclusion

Photonic integrated circuits are driven by the increasing requirements in bandwidth of communication networks. The potential for low energy consumption boosts its importance as an economical and effective solution compatible with electronics. The development of the optoelectronic devices is oriented toward large-scale integrated chips, and BP-integrated photonic circuits are considered to be a strategy to increase the integration level. The unique optical properties of BP offer new opportunities and promote new applications. We review the main applications of BP-integrated photonics including photodetection, modulation, light emission, and polarization conversion.

The BP-integrated photodetector exploits different photoelectric effects and provides wide operation bandwidth from visible to mid-IR on various substrates to match different application requirements. As for BP modulators, more efforts are needed to improve the electron–photon conversion, modulation efficiency, and response speed. BP light emitters have been demonstrated recently. The optimization of the device geometry and structure is an effective approach to enhance light–matter interaction and thus increasing efficiency. BP for polarization conversion is new and provides a new strategy to manipulate polarization in the mid-IR. The degradation of BP due to oxygen, water, and light is no longer a limiting factor since it could be effectively prevented by encapsulation and packaging.

Overall, BP-integrated photonic circuits have attracted considerable attention, and many advances have been achieved in

diverse aspects, such as theoretical study, material synthesis, integration methods, encapsulation strategy, and structural design. BP-based photonic devices have considerable potentials, while there are still some challenges for high-performance photonic integrated circuits. Considering the rapid development of synthesis and fabrication techniques, the development of BP-based optoelectronic devices will keep a fast pace.

Acknowledgments

Funding: This work was supported in part by the National Key Research and Development Program of China under Grant 2019YFB2205303, in part by the National Natural Science Foundation of China under Grant 62205054, in part by the Natural Science Foundation of Jiangsu Province under Grant BK20210207, and in part by the Fundamental Research Funds for the Central Universities. **Author contributions:** J.W. conceived the idea for the project. M.Z. and L.Y. collected the data. M.Z. and X.W. drafted the manuscript and J.W. revised. All authors gave final approval of the version to be published and have contributed to the manuscript. **Competing interests:** The authors declare that they have no competing interests.

Data Availability

The data could be given upon reasonable request from the corresponding authors.

References

1. Atabaki AH, Moazeni S, Pavanello F, Gevorgyan H, Notaros J, Alloatti L, Wade MT, Sun C, Kruger SA, Meng H, et al. Integrating photonics with silicon nanoelectronics for the next generation of systems on a chip. *Nature*. 2018;556(7701):349–354.
2. Feldmann J, Youngblood N, Karpov M, Gehring H, Li X, Stappers M, Le Gallo M, Fu X, Lukashchuk A, Raja AS, et al. Parallel convolutional processing using an integrated photonic tensor core. *Nature*. 2021;589(7840):52–58.
3. Grotevent MJ, Yakunin S, Bachmann D, Romero C, Vazquez A, Madi M, Calame M, Kovalenko MV, Shorubalko I. Integrated photodetectors for compact fourier-transform waveguide spectrometers. *Nat Photonics*. 2023;17(1):59–64.
4. Fang JR, Liu D, Xu DX, Wu QN, Li HB, Li Y, Hu N. Integrated Au-nanoroded biosensing and regulating platform for photothermal therapy of bradyarrhythmia. *Research*. 2022;2022:Article 9854342.
5. Milvich J, Kohler D, Freude W, Koos C. Integrated phase-sensitive photonic sensors: A system design tutorial. *Adv Opt Photonics*. 2021;13(3):584–642.
6. Pintus P, Ranzani L, Pinna S, Huang D, Gustafsson MV, Karinou F, Casula GA, Shoji Y, Takamura Y, Mizumoto T, et al. An integrated magneto-optic modulator for cryogenic applications. *Nat Electron*. 2022;5(9):604–610.
7. Li Z, Xue J, Cea MD, Kim JW, Nong H, Chong D, Lim KY, Quek E, Ram RJ. A sub-wavelength Si LED integrated in a CMOS platform. *Nat Commun*. 2023;14(1):Article 882.
8. Novoselov KS, Geim AK, Morozov SV, Jiang D, Zhang Y, Dubonos SV, Grigorieva IV, Firsov AA. Electric field effect in atomically thin carbon films. *Science*. 2004;306(5696):666–669.
9. Maiti R, Patil C, Saadi M, Xie T, Azadani JG, Uluutku B, Amin R, Briggs AF, Miscuglio M, Van TD, et al. Strain-engineered high-responsivity $MoTe_2$ photodetector for silicon photonic integrated circuits. *Nat Photonics*. 2020;14(9):578–584.
10. Peyskens F, Chakraborty C, Muneeb M, Van TD, Englund D. Integration of single photon emitters in 2D layered materials with a silicon nitride photonic chip. *Nat Commun*. 2019;10(1):Article 4435.
11. Xu ZF, Tang BS, Zhang XY, Leong JF, Pan JM, Hooda S, Zamburg E, Thean AV-Y. Reconfigurable nonlinear photonic activation function for photonic neural network based on non-volatile opto-resistive ram switch. *Light Sci Appl*. 2022;11(1):Article 288.
12. Fang HL, Liu J, Lin QL, Su RB, Wei YM, Krauss TF, Li JT, Wang Y, Wang XH. Laser-like emission from a sandwiched $MoTe_2$ heterostructure on a silicon single-mode resonator. *Adv Opt Mater*. 2019;7(20):Article 1900538.
13. Sim U, Moon J, Lee J, An J, Ahn HY, Kim DJ, Jo I, Jeon C, Han S, Hong BH, et al. Double-layer graphene outperforming monolayer as catalyst on silicon photocathode for hydrogen production. *ACS Appl Mater Interfaces*. 2017;9(4):3570–3580.
14. Xuan YF, Chen H, Chen Y, Zheng HN, Lu YH, Lin SS. Graphene/semiconductor heterostructure wireless energy harvester through hot electron excitation. *Research*. 2020;2020:Article 3850389.
15. Choi MS, Nipane A, Kim BSY, Ziffer ME, Datta I, Borah A, Jung Y, Kim B, Rhodes D, Jindal A, et al. High carrier mobility in graphene doped using a monolayer of tungsten oxyselenide. *Nat Electron*. 2021;4(10):731–739.
16. Sun JY, Chen ZL, Yuan L, Chen YB, Ning J, Liu SW, Ma DL, Song XJ, Priydarshi MK, Bachmatiuk A, et al. Direct chemical-vapor-deposition-fabricated, large-scale graphene glass with high carrier mobility and uniformity for touch panel applications. *ACS Nano*. 2016;10(12):11136–11144.
17. Estrada D, Li ZY, Choi G-M, Dunham SN, Serov A, Lee J, Meng Y, Lian F, Wang NC, Perez A, et al. Thermal transport in layer-by-layer assembled polycrystalline graphene films. *npj 2D Mater Appl*. 2019, 3(1):Article 10.
18. Sun ZP, Martinez A, Wang F. Optical modulators with 2D layered materials. *Nat Photonics*. 2016;10(4):227–238.
19. Yuan SF, Naveh D, Watanabe K, Taniguchi T, Xia FN. A wavelength-scale black phosphorus spectrometer. *Nat Photonics*. 2021;15(8):601–607.
20. Li B, Zhang YN, Fu L, Zhang LY, Liu ZY, Yin LW. Two-dimensional black phosphorous induced exciton dissociation efficiency enhancement for high-performance all-inorganic $CsPbI_3$ perovskite photovoltaics. *J Mater Chem A*. 2019;7(39):22539–22549.
21. Yang LP, Shen T, Lim YV, Pam ME, Guo L, Shi YM, Yang HY. Design of black phosphorous derivatives with excellent stability and ion-kinetics for alkali metal-ion battery. *Energy Stor Mater*. 2021;35:283–309.
22. Shen ZK, Yuan YJ, Pei L, Yu ZT, Zou ZG. Black phosphorus photocatalysts for photocatalytic H_2 generation: A review. *Chem Eng J*. 2020;386(15):Article 123997.
23. Aslan E, Eroğlu Z, Yanalak G, Metin Ö, Hatay PI. Enhanced hydrogen evolution via in situ generated 2D black phosphorous nanocomposites at the liquid/liquid interfaces. *Appl Surf Sci*. 2022;604:Article 154435.
24. Hao CX, Wen FS, Xiang JY, Yuan SJ, Yang BC, Li L, Wang WH, Zeng ZM, Wang LM, Liu ZY, et al. Liquid-exfoliated black phosphorous nanosheet thin films for flexible resistive

random access memory applications. *Adv Funct Mater*. 2016;26(12):2016–2024.
25. Pandey A, Nikam AN, Padya BS, Kulkarni S, Fernandes G, Shreya AB, García MC, Caro C, Páez-Muñoz JM, Dhas N, et al. Surface architectured black phosphorous nanoconstructs based smart and versatile platform for cancer theranostics. *Coord Chem Rev*. 2021;435(15):Article 213826.
26. Donskyi IS, Huang X, Wichmann N, Bawadkji O, Ahmed R, Nickl P, Herziger S, Radnik J, Achazi K, Qiao H, et al. Polylactide-block-polyglycerol-functionalized black phosphorous nanosheets for tumor therapy. *ACS Appl Nano Mater*. 2022;5(9):13417–13424.
27. Bridgman P. Two new modifications of phosphorus. *J Am Chem Soc*. 1914;36(7):1344–1363.
28. Xia FN, Wang H, Jia YC. Rediscovering black phosphorus as an anisotropic layered material for optoelectronics and electronics. *Nat Commun*. 2014;5:Article 4458.
29. Chen C, Lu XB, Deng BC, Chen XL, Guo QS, Li C, Ma C, Yuan SF, Sung E, Watanabe KJ, et al. Widely tunable mid-infrared light emission in thin-film black phosphorus. *Sci Adv*. 2020;6(7):Article aay6134.
30. Cao Y, Li CZ, Deng J, Tong T, Yc Q, Zhan GX, Zhang X, He KY, Ma HF, Zhang JR, et al. Enhanced photodetector performance of black phosphorus by interfacing with chiral perovskite. *Nano Res*. 2022;15(8):7492–7497.
31. Koleśnik-Gray M, Meingast L, Siebert M, Unbehaun T, Huf T, Ellrott G, Abellán G, Wild S, Lloret V, Mundloch U, et al. Unconventional conductivity increase in multilayer black phosphorus. *npj 2D Mater Appl*. 2023;7(1):Article 21.
32. Chen C, Yin YL, Zhang RC, Yuan QH, Xu Y, Zhang YS, Chen J, Zhang Y, Li C, Wang JY, et al. Growth of single-crystal black phosphorus and its alloy films through sustained feedstock release. *Nat Mater*. 2023;22(6):717–724.
33. Huang H, Jiang B, Zou XM, Zhao XZ, Liao L. Black phosphorus electronics. *Sci Bull*. 2019;64(15):1067–1079.
34. Long MS, Gao AY, Wang P, Xia H, Ott C, Pan C, Fu YJ, Ef L, Chen XS, Lu W, et al. Room temperature high-detectivity mid-infrared photodetectors based on black arsenic phosphorus. *Sci Adv*. 2017;3(6):Article e1700589.
35. Endo S, Akahama Y, Terada S, Narita S. Growth of large single crystals of black phosphorus under high pressure. *Jpn J Appl Phys*. 1982;21:L482–L484.
36. Yang ZB, Hao JH, Yuan SG, Lin SH, Yau HM, Dai JY, Lau SP. Field-effect transistors based on amorphous black phosphorus ultrathin films by pulsed laser deposition. *Adv Mater*. 2015;27(25):3748–3754.
37. Yu Y, Xing B, Wang D, Guan L, Niu XY, Yao JD, Yan XY, Zhang SC, Liu YL, Wu XX, et al. Improvement in the quality of black phosphorus by selecting a mineralizer. *Nanoscale*. 2019;11(42):20081–20089.
38. Wang YJ, Yu Q, Li J, Wang JY, Zhang K. Insight into the growth mechanism of black phosphorus. *Front Phys*. 2023;18:Article 43603.
39. Yang LS, Wang DS, Liu MS, Liu HM, Tan JY, Wang ZY, Zhou HY, Yu QM, Wang JY, Lin JH, et al. Glue-assisted grinding exfoliation of large-size 2D materials for insulating thermal conduction and large-current-density hydrogen evolution. *Mater Today*. 2021;51:145–154.
40. Zhang C, Tan JY, Pan YK, Cai XK, Zou XL, Cheng HM, Liu BL. Mass production of 2D materials by intermediate-assisted grinding exfoliation. *Natl Sci Rev*. 2020;7(2):324–332.
41. Lk L, Kim J, Jin CH, Ye GJ, Qiu DY, da Jornada FH, Shi ZW, Chen L, Zhang ZC, Yang FY, et al. Direct observation of the layer-dependent electronic structure in phosphorene. *Nat Nanotechnol*. 2017;12(1):21–25.
42. Qiao JS, Kong XH, Hu ZX, Yang F, Ji W. High-mobility transport anisotropy and linear dichroism in few-layer black phosphorus. *Nat Commun*. 2014;5:Article 4475.
43. Jw Y, Tran S, Wu J, Che S, Stepanov P, Taniguchi T, Watanabe K, Baek H, Smirnov D, Chen R, et al. Integer and fractional quantum hall effect in ultrahigh quality few-layer black phosphorus transistors. *Nano Lett*. 2018;18(1):229–234.
44. Chen XL, Wu YY, Wu ZF, Han Y, Xu SG, Wang WG, Ye W, Han TY, He YH, Cai Y, et al. High-quality sandwiched black phosphorus heterostructure and its quantum oscillations. *Nat Commun*. 2015;6:Article 7315.
45. Wang H, Wang XM, Xia FN, Wang LH, Jiang H, Xia QF, Chin ML, Dubey M, Han SJ. Black phosphorus radio-frequency transistors. *Nano Lett*. 2014;14(11):6424–6429.
46. Wu SQ, Chen Y, Wang XD, Jiao HX, Zhao QR, Huang XN, Tai XC, Zhou Y, Chen H, Wang XJ, et al. Ultra-sensitive polarization-resolved black phosphorus homojunction photodetector defined by ferroelectric domains. *Nat Commun*. 2022;13(1):Article 3198.
47. Jeon SG, Shin H, Jaung YH, Ahn J, Song JY. Thickness-dependent and anisotropic thermal conductivity of black phosphorus nanosheets. *Nanoscale*. 2018;10(13):5985–5989.
48. Wang FJ, Xu YG, Mu L, Zhang JS, Xia W, Xue JM, Guo YF, Yang JH, Yan HG. Anisotropic infrared response and orientation-dependent strain-tuning of the electronic structure in Nb_2SiTe_4. *ACS Nano*. 2022;16(5):8107–8115.
49. Zheng JL, Yang ZH, Chen S, Liang ZM, Chen X, Cao R, Za G, Wang K, Zhang Y, Ji JH, et al. Black phosphorus based all-optical-signal-processing toward high performances and enhanced stability. *ACS Photonics*. 2017;4(6):1466–1476.
50. Lien MR, Wang N, Wu J, Soibel A, Gunapala SD, Wang H, Povinelli ML. Resonant grating-enhanced black phosphorus mid-wave infrared photodetector. *Nano Lett*. 2022;22(21):8704–8710.
51. He MJ, Qi H, Ren YT, Zhao YJ, Zhang Y, Shen JD, Antezza M. Radiative thermal switch driven by anisotropic black phosphorus plasmons. *Opt Express*. 2020;28(18):26922–26934.
52. Zhang R, Zhang Y, Yu H, Zhang H, Yang R, Yang B, Liu Z, Wang J. Broadband black phosphorus optical modulator in the spectral range from visible to mid-infrared. *Adv Optical Mater*. 2015;3(12):1787–1792.
53. Huang YQ, Ning JQ, Chen HM, Xu YJ, Wang X, Ge XT, Jiang C, Zhang X, Zhang JW, Peng Y, et al. Mid-infrared black phosphorus surface-emitting laser with an open microcavity. *ACS Photonics*. 2019;6(7):1581–1586.
54. Ryder CR, Wood JD, Wells SA, Yang Y, Jariwala D, Marks TJ, Schatz GC, Hersam MC. Covalent functionalization and passivation of exfoliated black phosphorus via aryl diazonium chemistry. *Nat Chem*. 2016;8(6):597–602.
55. Abate Y, Akinwande D, Gamage S, Wang H, Snure M, Poudel N, Cronin SB. Recent progress on stability and passivation of black phosphorus. *Adv Mater*. 2018;30(29):Article e1704749.
56. Clark N, Nguyen L, Hamer MJ, Schedin F, Lewis EA, Prestat E, Garner A, Cao Y, Zhu M, Kashtiban R, et al. Scalable patterning of encapsulated black phosphorus. *Nano Lett*. 2018;18(9):5373–5381.

57. Qu ZC, Wu K, Meng WH, Nan BG, Hu ZR, Xu CA, Tan ZY, Zhang Q, Meng HF, Shi J. Surface coordination of black phosphorene for excellent stability, flame retardancy and thermal conductivity in epoxy resin. *Chem. Eng J*. 2020;397:Article 125416.
58. Chang YK, Nie A, Yuan SJ, Wang BC, Mu CP, Xiang JY, Yang BC, Li L, Wen FS, Liu ZY. Liquid-exfoliation of S-doped black phosphorus nanosheets for enhanced oxygen evolution catalysis. *Nanotechnology*. 2019;30(3):Article 035701.
59. Plutnar J, Šturala J, Mazánek V, Sofer Z, Pumera M. Fluorination of black phosphorus-will black phosphorus burn down in the elemental fluorine? *Adv Funct Mater*. 2018;28(35):Article 1801438.
60. Wild S, Dinh XT, Maid H, Hauke F, Abellan G, Hirsch A. Quantifying the covalent functionalization of black phosphorus. *Angew Chem Int Edit*. 2020;59(45):20230–20234.
61. Liu MQ, Feng SM, Hou Y, Zhao SL, Tang L, Liu JM, Wang F, Liu BL. High yield growth and doping of black phosphorus with tunable electronic properties. *Mater Today*. 2020;36:91–101.
62. Hideo A, Akira M. Band structure and optical properties of black phosphorus. *J Phys Solid State Phys*. 1984;17(11):1839–1852.
63. Ling X, Wang H, Huang SX, Xia FN, Dresselhaus MS. The renaissance of black phosphorus. *P Natl Acad Sci USA*. 2015;112(15):4523–4530.
64. Castellanos-Gomez A. Black phosphorus: Narrow gap, wide applications. *J Phys Chem Lett*. 2015;6(21):4280–4291.
65. Hideo A, Koichi S, Akira M. Electronic structure of black phosphorus in self-consistent pseudopotential approach. *J Phys Soc Jpn*. 1982;51:1193–1199.
66. Yukihiro T, Hideo A, Akira M. Electronic structure of black phosphorus in tight binding approach. *J Phys Soc Jpn*. 1981;105:93–98.
67. Deng BC, Tran V, Xie YJ, Jiang H, Li C, Guo QS, Wang XM, Tian H, Koester SJ, Wang H, et al. Efficient electrical control of thin-film black phosphorus bandgap. *Nat Commun*. 2017;8:14474.
68. Han L, Adam TN, Zhen Z, Zhe L, Xu X, David T, Peide DY. Phosphorene: An unexplored 2D semiconductor with a high hole mobility. *ACS Nano*. 2014;8(4):4033–4041.
69. Castellanos-Gomez A, Vicarelli L, Prada E, Island JO, Narasimha-Acharya KL, Blanter SI, Groenendijk DJ, Buscema M, Steele GA, Alvarez JV, et al. Isolation and characterization of few-layer black phosphorus. *2D Mater*. 2014;1(2):Article 025001.
70. Tran V, Soklaski R, Liang Y, Yang L. Layer-controlled band gap and anisotropic excitons in few-layer black phosphorus. *Phys Rev B*. 2014;89(23):Article 235319.
71. Wang XM, Jones AM, Seyler KL, Tran V, Jia YC, Zhao H, Wang H, Yang L, Xu XD, Xia FN. Highly anisotropic and robust excitons in monolayer black phosphorus. *Nat Nanotechnol*. 2015;10(6):517–521.
72. Yang J, Xu RJ, Pei JJ, Myint YW, Wang F, Wang Z, Zhang S, Yu Z, Lu Y. Optical tuning of exciton and Trion emissions in monolayer phosphorene. *Light Sci Appl*. 2015;4(7):Article e312.
73. Zhang CD, Lian JC, Yi W, Jiang YH, Liu LW, Hu H, Xiao WD, Du SX, Sun LL, Gao HJ. Surface structures of black phosphorus investigated with scanning tunneling microscopy. *J Phys Chem C*. 2009;113:18823–18826.
74. Liang LB, Wang J, Lin WZ, Sumpter BG, Meunier V, Pan M. Electronic bandgap and edge reconstruction in phosphorene materials. *Nano Lett*. 2014;14(11):6400–6406.
75. Liu BL, Kopf M, Abbas AN, Wang XM, Guo QS, Jia YC, Xia FN, Weihrich R, Bachhuber F, Pielnhofer F, et al. Black arsenic-phosphorus: Layered anisotropic infrared semiconductors with highly tunable compositions and properties. *Adv Mater*. 2015;27(30):4423–4429.
76. Lan SF, Rodrigues S, Kang L, Cai WS. Visualizing optical phase anisotropy in black phosphorus. *ACS Photonics*. 2016;3(7):1176–1181.
77. Wang XM, Lan SF. Optical properties of black phosphorus. *Adv in Opt Photonics*. 2016;8(4):618–655.
78. Ling X, Huang SX, Hasdeo EH, Liang LB, Parkin WM, Tatsumi Y, Nugraha ART, Puretzky AA, Das PM, Sumpter BG, et al. Anisotropic electron-photon and electron-phonon interactions in black phosphorus. *Nano Lett*. 2016;16(4):2260–2267.
79. Mao NN, Tang JY, Xie LM, Wu JX, Han BW, Lin JJ, Deng SB, Ji W, Xu H, Liu KH, et al. Optical anisotropy of black phosphorus in the visible regime. *J Am Chem Soc*. 2016;138(1):300–305.
80. Wu JX, Mao NN, Xie LM, Xu H, Zhang J. Identifying the crystalline orientation of black phosphorus using angle-resolved polarized raman spectroscopy. *Angew Chem Int Ed*. 2015;54(8):2366–2369.
81. Alodan SA, Gorham JM, DelRio FW, Alsaffar F, Aljalham G, Alolaiyan O, Zhou C, Amer MR. Room temperature wideband tunable photoluminescence of pulsed thermally annealed layered black phosphorus. *Nano*. 2020;9(14):4253–4264.
82. Wang JJ, Rousseau A, Eizner E, Phaneuf-L'Heureux A-L, Schue L, Francoeur S, Kéna-Cohen S. Spectral responsivity and photoconductive gain in thin film black phosphorus photodetectors. *ACS Photonics*. 2019;6(12):3092–3099.
83. Deckoff-Jones S, Lin H, Kita D, Zheng H, Li D, Zhang W, Hu J. Chalcogenide glass waveguide-integrated black phosphorus mid-infrared photodetectors. *J Opt*. 2018;20(4):Article 044004.
84. Huang L, Dong B, Guo X, Chang Y, Chen N, Huang X, Liao W, Zhu C, Wang H, Lee C, et al. Waveguide-integrated black phosphorus photodetector for mid-infrared applications. *ACS Nano*. 2019;13(1):913–921.
85. Yin YL, Cao R, Guo JS, Liu CY, Li J, Feng XL, Wang HD, Du W, Qadir A, Zhang H, et al. High-speed and high-responsivity hybrid silicon/black-phosphorus waveguide photodetectors at 2 μm. *Laser Photonics Rev*. 2019;13(6):Article 1900032.
86. Zha JJ, Luo MC, Ye M, Ahmed T, Yu X, Lien DH, He QY, Lei DY, Ho JC, Bullock J, et al. Infrared photodetectors based on 2D materials and nanophotonics. *Adv Func Mater*. 2021;32(15):2111970.
87. Koppens FH, Mueller T, Avouris P, Ferrari AC, Vitiello MS, Polini M. Photodetectors based on graphene, other two-dimensional materials and hybrid systems. *Nat Nanotechnol*. 2014;9(10):780–793.
88. Youngblood N, Che C, Koester JS, Li M. Waveguide-integrated black phosphorus photodetector with high responsivity and low dark current. *Nat Photonics*. 2015;9(4):247–252.
89. Ma YM, Dong BW, Wei JX, Chang YH, Huang L, Ang KW, Lee C. High-responsivity mid-infrared black phosphorus slow light waveguide photodetector. *Adv Opt Mater*. 2020;8(13):Article 2000337.
90. Liu CY, Guo JS, Yu LW, Xiang YL, Xiang HT, Li J, Dai DX. High-speed and high-responsivity silicon/black-phosphorus hybrid plasmonic waveguide avalanche photodetector. *ACS Photonics*. 2022;9(5):1764–1774.

91. Chen PL, Chen Y, Chang TY, Li WQ, Li JX, Lee S, Fang Z, Li M, Majumdar A, Liu CH. Waveguide-integrated van der waals heterostructure mid-infrared photodetector with high performance. *ACS Appl Mater Interfaces*. 2022;14(21): 24856–24863.
92. Xue Y, Wu XX, Chen KX, Wang JJ, Liu L. Waveguide integrated high-speed black phosphorus photodetector on a thin film lithium niobate platform. *Opt Mater Express*. 2022;13(1):272–281.
93. Sasikala V, Chitra K. All optical switching and associated technologies: A review. *J Opt*. 2018;47(3):307–317.
94. Xu H, Ding BF, Xu YA, Huang ZY, Wei DH, Chen SH, Lan TS, Pan YK, Cheng HM, Liu BL. Magnetically tunable and stable deep-ultraviolet birefringent optics using two-dimensional hexagonal boron nitride. *Nat Nanotechnol*. 2022;17(10): 1091–1096.
95. Shang C, Zhang YB, Qin HY, He BQ, Zhang CH, Sun JX, Li J, Ma JG, Ji XM, Xu LJ, et al. Review on wavelength-tunable pulsed fiber lasers based on 2D materials. *Opt Laser Technol*. 2020;131:Article 106375.
96. Li D, Castillo AE, Jussila H, Ye G, Ren Z, Bai J, Chen X, Lipsanen H, Sun Z, Bonaccorso F. Black phosphorus polycarbonate polymer composite for pulsed fibre lasers. *Appl Mater Today*. 2016;4:17–23.
97. Paschotta R. *Encyclopedia of laser physics and technology.* New York (USA): Wiley-VCH; 2008.
98. Huang JW, Dong NN, Zhang SF, Sun ZY, Zhang WH, Wang J. Nonlinear absorption induced transparency and optical limiting of black phosphorus nanosheets. *ACS Photonics*. 2017;4(12):3063–3070.
99. Wang YZ, Zhang F, Tang X, Chen X, Chen YX, Huang WC, Liang ZM, Wu LM, Ge YQ, Song YF, et al. All-optical phosphorene phase modulator with enhanced stability under ambient conditions. *Laser Photonics Rev*. 2018;12(6):Article 1800016.
100. Cheng Z, Cao R, Guo J, Yao YH, Wei KK, Gao S, Wang YZ, Dong JJ, Zhang H. Phosphorene-assisted silicon photonic modulator with fast response time. *Nano*. 2020;9(7):1973–1979.
101. Pollock CR, Lipson M. *Integrated photonics*. New York (USA): Kluwer Academic Publishers; 2003.
102. Miller DA, Chemla DS, Schmitt-Rink S. Relation between electroabsorption in bulk semiconductors and in quantum wells: The quantum-confined Franz-Keldysh effect. *Phys Rev B Condens Matter*. 1986;33(10):6976–6982.
103. Moss TS. The interpretation of the properties of indium antimonide. *P Phys Soc B*. 1954;67(48):775–782.
104. Burstein E. Anomalous optical absorption limit in insb. *Phys Rev*. 1954;93(3):632–633.
105. Liu YP, Qiu ZZ, Carvalho A, Bao Y, Xu H, Tan SJ, Liu W, Castro Neto AH, Loh KP, Lu J. Gate-tunable giant stark effect in few-layer black phosphorus. *Nano Lett*. 2017;17(3):1970–1977.
106. Peng R, Khaliji K, Youngblood N, Grassi R, Low T, Li M. Midinfrared electro-optic modulation in few-layer black phosphorus. *Nano Lett*. 2017;17(10):6315–6320.
107. Lin C, Grassi R, Low T, Helmy AS. Multilayer black phosphorus as a versatile mid-infrared electro-optic material. *Nano Lett*. 2016;16(3):1683–1689.
108. Huang L, Dong B, Yu ZG, Zhou J, Ma Y, Zhang YW, Lee C, Ang KW. Mid-infrared modulators integrating silicon and black phosphorus photonics. *Mater Today Adv*. 2021;12:Article 100170.
109. Deng W, Jin XC, Lv Y, Zhang XJ, Zhang XH, Jie JS. 2D ruddlesden-popper perovskite nanoplate based deep-blue light-emitting diodes for light communication. *Adv Funct Mater*. 2019;29(40):1903861.
110. Jung H, Sim S, Lee H. Biometric authentication security enhancement under quantum dot light-emitting diode display via fingerprint imaging and temperature sensing. *Sci Rep*. 2023;13(1):794.
111. Fuji K, Neba Y. Electromagnetic interference of using 24Vdc current control buck converter for medical light emitting diode. *Energy Rep*. 2020;6:1325–1330.
112. Li D, Xu JR, Ba K, Xuan NN, Chen MY, Sun ZZ, Zhang YZ, Zhang ZX. Tunable bandgap in few-layer black phosphorus by electrical field. *2D Mater*. 2017;4(3):Article 031009.
113. Azar NS, Bullock J, Balendhran S, Kim H, Javey A, Crozier KB. Light-matter interaction enhancement in anisotropic 2D black phosphorus via polarization-tailoring nano-optics. *ACS Photonics*. 2021;8(4):1120–1128.
114. Wang JJ, Rousseau A, Yang M, Low T, Francoeur S, Kéna-Cohen S. Mid-infrared polarized emission from black phosphorus light-emitting diodes. *Nano Lett*. 2020;20(5):3651–3655.
115. Chang TY, Chen Y, Luo DI, Li JX, Chen PL, Lee S, Fang Z, Li WQ, Zhang YY, Li M, et al. Black phosphorus mid-infrared light-emitting diodes integrated with silicon photonic waveguides. *Nano Lett*. 2020;20(9):6824–6830.
116. Kim H, Uddin SZ, Lien DH, Yeh M, Azar NS, Balendhran S, Kim T, Gupta N, Rho Y, Grigoropoulos CP, et al. Actively variable-spectrum optoelectronics with black phosphorus. *Nature*. 2021;596(7871):232–237.
117. Chen C, Chen F, Chen XL, Deng BC, Eng B, Jung D, Guo QS, Yuan SF, Watanabe K, Taniguchi T, et al. Bright mid-infrared photoluminescence from thin-film black phosphorus. *Nano Lett*. 2019;19(3):1488–1493.
118. Zong XR, Hu HM, Ouyang G, Wang JW, Shi R, Zhang L, Zeng QS, Zhu C, Chen SH, Cheng C, et al. Black phosphorus-based van der waals heterostructures for mid-infrared light-emission applications. *Light Sci Appl*. 2020;9:Article 114.
119. Gupta N, Kim H, Azar NS, Uddin SZ, Lien DH, Crozier KB, Javey A. Bright mid-wave infrared resonant-cavity light-emitting diodes based on black phosphorus. *Nano Lett*. 2022;22(3):1294–1301.
120. Chen PL, Chang TY, Chen PS, Chan AHY, Rosyadi AS, Lin YJ, Huang PY, Li JX, Li WQ, Hsu CJ, et al. Van der waals heterostructure mid-infrared emitters with electrically controllable. *ACS Nano*. 2023;17(11): 10181–10190.
121. Biswas S, William SW, Grajowe MY, Watanab EK, Taniguchi T, Bechtel HA, Rossman GA, Atwater H. Tunable intraband optical conductivity and polarization-dependent epsilon-near-zero behavior in black phosphorus. *Sci Adv*. 2021;7:eabd4623.
122. Chen ZY, Yan LS, Pan Y, Jiang L, Yi AL, Pan W, Luo B. Use of polarization freedom beyond polarization-division multiplexing to support high-speed and spectral-efficient data transmission. *Light Sci Appl*. 2016;6(2):Article e16207.
123. Tang PJ, Kirby MA, Le N, Li YD, Zeinstra N, Lu GN, Murry CE, Zheng Y, Wang RK. Polarization sensitive optical coherence tomography with single input for imaging depth-resolved collagen organizations. *Light Sci Appl*. 2021;10(1):Article 237.
124. Xiong W, Hsu CW, Bromberg Y, Antonio-Lopez JE, Amezcua Correa R, Cao H. Complete polarization control in

multimode fibers with polarization and mode coupling. *Light Sci Appl*. 2018;7:54.
125. Hsu C, Xu ZD, Wang XG. Symmetry-breaking response of azo molecular glass microspheres to interfering circularly polarized light: From shape manipulation to 3D patterning. *Adv Funct Mater*. 2019;29(3):Article 1806703.
126. Biswas S, Grajower MY, Watanabe K, Taniguchi T, Atwater HA. Broadband electro-optic polarization conversion with atomically thin black phosphorus. *Science*. 2021;374(6566):448–453.
127. Matthaiakakis N, Droulias S, Kakarantzas G. Dynamic control of light chirality with nanostructured monolayer black phosphorus for broadband terahertz applications. *Adv Opt Mater*. 2022;10(5):Article 2102273.
128. Hu H, Geng MX, Jiang ZQ, Zhang H, Zhu Z, Guan CY, Zhang H, Shi JH. Tunable circular polarization responses of twisted black phosphorus metamaterials. *Opt Express*. 2022;30(26):Article 47690.
129. Bao WZ, Liu L, Wang CY, Choi S, Wang D, Wang GX. Solar cells: Facile synthesis of crumpled nitrogen-doped mxene nanosheets as a new sulfur host for lithium-sulfur batteries. *Adv Energy Mater*. 2018;8(13):Article 1870060.
130. Parto K, Azzam SI, Lewis N, Patel SD, Umezawa S, Watanabe K, Taniguchi T, Moody G. Cavity-enhanced 2D material quantum emitters deterministically integrated with silicon nitride microresonators. *Nano Lett*. 2022;22(23):9748–9756.
131. Li WY, Guo YM, Luo ZP, Wu SH, Han B, Hu WJ, You L, Kj W, Taniguchi T, Alava T, et al. A gate programmable van der waals metal-ferroelectric-semiconductor vertical heterojunction memory. *Adv Mater*. 2023;35(5):Article e2208266.
132. Kim Y, Lee S, Song JG, Ko KY, Woo WJ, Lee SW, Park M, Lee H, Lee Z, Choi H, et al. 2D transition metal dichalcogenide heterostructures for p- and n-type photovoltaic self-powered gas sensor. *Adv Funct Mater*. 2020;30(43):Article 2003360.